Ab Initio Study of CO Hydrogenation to Oxygenates on Reduced Rh Terraces and Stepped Surfaces

Neeti Kapur,[*,†] **Jangsuk Hyun,**[†] **Bin Shan,**[†] **John B. Nicholas,**[†] **and Kyeongjae Cho**[*,‡]

Nanostellar Inc., 3696 Haven Avenue, Redwood City, California 94063, and Department of Material Science and Engineering and Department of Physics, University of Texas at Dallas, Richardson, Texas 75080

Previously reported syngas conversion experiments on silica-supported Rh nanoparticles show that CO conversion and oxygenate selectivity vary as a function of nanoparticle size. Theoretical studies in the literature have examined the effect of steps on CO dissociation, but structure sensitivity for C_1 and C_2 oxygenates has not been systematically investigated. In this study, density functional theory-based reaction energetics and kinetics for C−H, C−C, C−O, and O−H bond formation on flat Rh(111) and stepped Rh(211) surfaces are reported and compared. Multiple paths for methanol and ethanol formation are considered to ascertain the lowest energy pathways. Nearly an identical methanol formation route via $CO \rightarrow CHO \rightarrow CH_2O \rightarrow CH_3O \rightarrow CH_3OH$ is found to be favored on both Rh terrace and (211) sites. CO insertion into CH_2 is deduced to be the precursor for C_2 oxygenate formation irrespective of site structure. Ethanol formation pathways, however, are determined to be markedly different on flat and stepped Rh surfaces in terms of barriers and intermediates. Our results show that reaction pathways are typically preferred on Rh step sites irrespective of the bond-breaking and -making (C−H, C−C, and C−O) reactions considered.

Introduction

Industrial synthesis of hydrocarbons and oxygenates from syngas requires active catalysts with high product selectivity;[1,2] therefore, a comprehensive understanding of the catalytic cycle on existing materials is essential for further material development. Rh catalysts have shown moderate activity and good selectivity toward oxygenates due to their unique ability to dissociate carbon monoxide (CO) while ensuring CO insertion.[3] Quyoum et al.[4] report selective methanol (CH_3OH) and ethanol (CH_3CH_2OH) formation on silica-supported Rh in addition to methane, C_2, and C_3 hydrocarbons. X-ray photoelectron spectroscopic (XPS) studies indicate that Rh on silica supports exists in between metallic Rh and Rh_2O_3 states.[5] Temperature-programmed H_2 reduction (TPR) corresponds to a maximum at a temperature of 420 K on these Rh/SiO_2 surfaces.[5] Because operating temperatures (450−770 K) for the syngas conversion process are in excess of H_2 reduction temperature, silica-supported Rh is deduced to be in reduced form under reaction conditions. Ichikawa and co-workers[6,7] have previously hypothesized that Rh^0 sites are responsible for CO dissociation, while $Rh^{\delta+}$ sites ensure CO insertion for promoted Rh and oxidic supports. Under high temperatures, however, infrared spectroscopic investigations on unpromoted and promoted Rh catalysts conclude that gem-dicarbonyls [$Rh^+(CO)_2$] produced on cationic Rh reduce to $Rh^0(CO)$.[7−11] We, therefore, constrain our efforts to reduced Rh surfaces for the purpose of this study and focus on how site structure affects dominant CO conversion pathways to oxygenates.

Defect formation under high temperature and pressure and in the presence of syngas is likely on Rh-based catalysts analogous to other Fischer−Tropsch (FT) catalysts.[12−14] Un-

dercoordinated islands forming these defects can be attributed to mobile Rh subcarbonyls detected on single crystals[15] and supported Rh surfaces.[16] Particle size studies undertaken for Rh nanoparticles[17−19] show variance in catalytic activity and selectivity, which indicates sensitivity to site structure. Arakawa et al.[17] have reported an increase in CO turnover frequency (TOF) as the silica-supported Rh nanoparticle size increases from 2 to 6 nm, confirmed by other groups. CH_3OH is formed selectively on small particles (<2 nm), while methane and acetaldehyde (CH_3CHO) are favored on large (∼6 nm) nanoparticles. Medium-sized particles (∼2−3.5 nm) correspond to maximum selectivity for CH_3CH_2OH. Bao and co-workers attribute high TOF to fast CO dissociation on large Rh/SiO_2 nanoparticles.[19] Stacking faults have been observed in transmission electron microscopy images for 5 nm Rh nanoparticles on alumina supports, suggesting an increase in the step density with nanoparticle size.[20] CO dissociation enhancement on defects has been confirmed with spectroscopic[21] and microscopic measurements on Rh clusters[22,23] and kinked step edges,[24−26] supported by theoretical simulations.[27,28] Despite the indication that Rh step sites are responsible for catalytic activity, the effect of site structure on CO hydrogenation mechanisms to oxygenates has not been explicitly examined.

^{12}CO and ^{13}C hydrogenated on Rh−Ti/SiO_2 produce unlabeled $^{12}CH_3OH$, while ^{13}C label is incorporated into the methyl (CH_3) group of CH_3CH_2OH and CH_3CHO,[6] indicating CH_3OH formation from undissociated CO. Takeuchi and Katzer[29] confirmed this finding by recording products of $^{12}C^{18}O$ and $^{13}C^{16}O$ hydrogenation on Rh and also ruled out CH_3OH homologation to higher oxygenates. The intermediate species involved in CO hydrogenation to CH_3OH on Rh are, however, unknown.

CO insertion reactions into methylene (CH_2) and CH_3 groups[30,31] have been considered previously as potential precursors for CH_3CH_2OH formation on Rh catalysts. Theoretical studies have invoked CO insertion into CH_3 for CH_3CH_2OH

* To whom correspondence should be addressed. E-mail: nkapur@nanostellar.com (N.K.) and kjcho@utdallas.edu (K.C.).
† Nanostellar Inc.
‡ University of Texas at Dallas.

10172 *J. Phys. Chem. C, Vol. 114, No. 22, 2010*

Kapur et al.

formation on Co surfaces[32] and Rh(111).[33] Experimentally, CH$_3$CHO has been considered to be a primary product on Rh surfaces, but conflicting conclusions have been deduced for CH$_3$CH$_2$OH formation. Mechanistic studies using ^{18}O distribution in CH$_3$CHO and CH$_3$CH$_2$OH derived from C^{18}O + H$_2$ reaction[34] show that CH$_3$CH$_2$OH is not formed by CH$_3$CHO hydrogenation. CH$_3$CHO adsorption on pure and Fe-promoted Rh shows no CH$_3$CH$_2$OH peaks and, therefore, supports the above-mentioned conclusions.[35] In contrast, Underwood and Bell[36] claim that CH$_3$CHO addition to CO hydrogenation experiments results in CH$_3$CH$_2$OH on oxide-supported Rh. Acetyl is, nevertheless, agreed upon as the common intermediate for CH$_3$CHO and CH$_3$CH$_2$OH due to similar formation rates obtained from ^{13}CO and ^{13}CH$_3$OH tracer studies.[6] IR peaks at 1658 cm^{-1} corresponding to adsorbed acyl on Rh nanoparticles[37] have been recorded and reported to stabilize as acetate ions.[37−39] The reactive intermediates leading to C$_2$ oxygenates are, therefore, not entirely resolved, and further insight into the mechanism is required for better understanding.

In this study, we investigate the above-mentioned concerns on the role of flat and stepped sites on catalytic cycles for C$_1$ and C$_2$ oxygenate formation. Comparisons are drawn between Rh(111) and Rh(211) surfaces to elucidate reactive intermediates, dominant reaction schemes, and preferential sites for product formation.

Computational Methodology

Ground state energies for the adsorbed systems were determined by using self-consistent, gradient-corrected density functional theory (DFT) as implemented in Vienna Ab-initio Simulation Package.[40] A three-layered slab was used to model a (2 × 2) unit cell of the Rh(111) surface with the metal atoms in the bottom layer fixed at the bulk positions.[33,41] The slab thickness used for Rh(111) was determined to be adequate for this investigation since energetic changes were less than 0.12 eV when five layers were included in the slab (Table 1 of the Supporting Information). The Rh(211) surface was modeled by an eight-layered slab for a (2 × 1) unit cell, and the atomic positions for the bottom three layers were kept fixed during the calculations. These nonspin-polarized calculations were run in cubic supercells with at least 10 Å of vacuum between the atoms in neighboring cells to ensure negligible interaction.

Plane waves with 400 eV as the cutoff energy were used to describe the electronic wave functions, and PAW pseudopotentials[42] were used to describe electron−ion interactions. The PW91 functional form of the generalized gradient approximation was used for calculating the exchange-correlation energies, and a 4 × 4 × 1 Monkhorst−Pack mesh was used for sampling the Brillouin zone for both of these surfaces.[43] Binding energies (BEs) were calculated by using the following equation:

$$BE = (E_{total} - E_{substrate} - E_{molecule}) + \Delta ZPE_{binding} \tag{1}$$

where E_{total} refers to the energy of total system, $E_{substrate}$ refers to the metal slab energy, $E_{molecule}$ refers to species in vacuum, and $\Delta ZPE_{binding}$ refers to the zero point energy (ZPE) correction. Vibrational frequencies for species in both the gas phase and the adsorbed state were used to determine ZPE corrections using eq 2.

$$\Delta ZPE_{binding} = \left(\sum_i^{mod\,es} \frac{h\nu_i}{2} \right)_{adsorbed} - \left(\sum_i^{mod\,es} \frac{h\nu_i}{2} \right)_{gas} \tag{2}$$

where h is Planck's constant and ν_i refers to frequency. Vibrational frequencies for adsorbed species were determined in single point calculations with metal atoms fixed at their positions. Frequencies greater than 200 cm^{-1} were included in the corrections since these have a nontrivial contribution to BE.

The dimer method[44] was used to find the transition state (TS) structures for reactions examined in this study, and the initial direction along the dimer was generated based on the reaction products. Imaginary frequencies were used to confirm these configurations, and the apparent activation barriers (E_a) were determined from eqs 3 and 4.

$$E_a = (E_{TS} - E_{IS}) + \Delta ZPE_{barrier} \tag{3}$$

where E_{TS} corresponds to the TS energy, E_{IS} refers to the reactant energy, and $\Delta ZPE_{barrier}$ refers to ZPE correction. For coadsorbed reactants, the reactant energy (E_{IS}) was calculated as the sum of individual BEs. ZPE correction for activation barrier was determined from the equation below

$$\Delta ZPE_{barrier} = \left(\sum_i^{mod\,es} \frac{h\nu_i}{2} \right)_{TS} - \left(\sum_i^{mod\,es} \frac{h\nu_i}{2} \right)_{IS} \tag{4}$$

where the first term includes vibrational frequencies for species in the TS and the second term includes vibrational frequencies for all of the adsorbed reactants. Imaginary frequencies for the TS are not included in this correction.

Results and Discussion

We first determined the adsorption energies for all of the relevant C$_x$H$_y$O$_z$ species involved in CO hydrogenation to CH$_3$OH and CH$_3$CH$_2$OH on Rh(111) and Rh(211). Subsequently, TSs were located for CO insertion and hydrogenation routes to oxygenates on both Rh surfaces.

Chemisorption Energies of Intermediates on Flat and Stepped Rh Surfaces. Figure 1a shows the four stable binding sites (atop, bridge, fcc, and hcp) examined on flat Rh surfaces. Side and top views for the Rh(211) surface with the (111) terrace and (100) step are shown in Figure 1b,c. Adsorption sites involving metal atoms on the step edge (atop, bridge, fcc, and hcp), lower edge (fcc and hcp), and (100) step (hollow sites) were examined on the Rh(211) surface. BEs and structural details for the lowest energy configurations of C$_x$H$_y$O$_z$ species are reported in Tables 1 and 2. ZPE corrections included in these binding values were determined to be significant for hydrogen atom, methoxy (CH$_3$O), and ethoxy intermediates (Table 2 of the Supporting Information).

Rh Terraces. CH$_3$OH and CH$_3$CH$_2$OH molecules adsorb on atop sites via their oxygen atoms, while atomic carbon, hydrogen, and oxygen prefer 3-fold hollow sites on a flat Rh surface. CH$_x$ products transition from 3-fold hollow sites for methylidyne (CH) to atop sites for CH$_3$. CH$_2$ binds equally strongly on both bridge and hcp sites.

CO adsorbs via C atom on atop sites. CH$_x$O (x = 1, 2) binds via both C and O atoms on the Rh surface, while CH$_3$O binds via its unsaturated oxygen atom on bridge sites. Hydroxy methyl (CH$_2$OH), hydroxy methylene (CHOH), and hydroxy methyli-
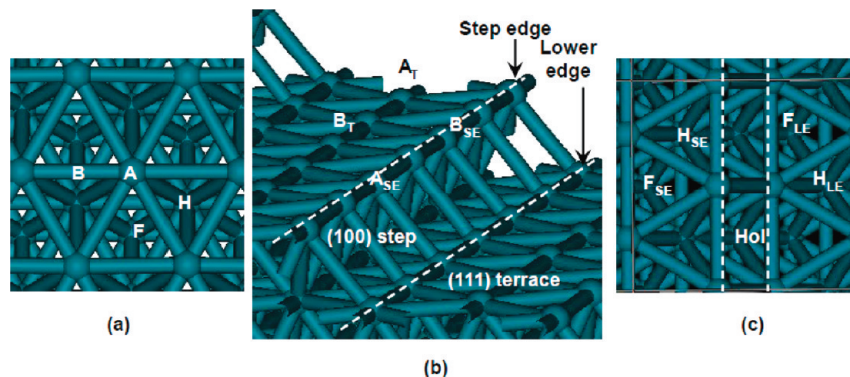
Figure 1. (a) Top view of the Rh(111) surface. A, B, F, and H refer to atop, bridge, fcc, and hcp adsorption sites on the flat surface. (b) Side view and (c) top view of the Rh(211) surface. A_{SE}, B_{SE}, F_{SE}, and H_{SE} refer to atop, bridge, fcc, and hcp sites on the step edge (SE). F_{LE} and H_{LE} refer to fcc and hcp sites on the lower edge (LE). A_T and B_T refer to atop and bridge sites on (111) terraces, and Hol refers to hollow adsorption sites on the stepped surface.

TABLE 1: BEs and Bond Distances (Rh–C and Rh–O) for Intermediates on the Rh(111) Surface[a]

species	BE (eV)	configuration	d_{Rh-C} (Å)	d_{Rh-O} (Å)
C	−7.13	hcp	1.917, 1.918, 1.920	
H	−2.59 (−0.49)	fcc	Rh–H: 1.866, 1.866, 1.886	
O	−5.02 (−1.95)	fcc		2.048, 2.048, 2.049
CO	−1.75	atop	1.850	
CH	−6.92	hcp	1.993, 1.994, 1.996	
CH_2	−3.86	bridge, hcp	2.046, 2.064	
CH_3	−1.74	atop	2.102	
OH	−3.07	bridge via O		2.198, 2.199, 2.228
CH_3OH	−0.28	atop via O		2.464
CH_3O	−2.18	bridge via O		2.168, 2.185
CH_2O	−0.84	C on atop and O on bridge over hcp site	2.108	2.228, 2.231
CHO	−2.40	both C and O on atop	1.946	2.253
CH_2OH	−1.79	atop via C	2.104	
CHOH	−3.18	bridge via C	2.064, 2.118	
COH	−4.43	hcp via C	2.011, 2.014, 2.021	
CH_3CHO	−0.53	both α-C and O on atop	2.203	2.085
CH_2CHO	−2.11	both β-C and O on atop	2.188	2.230
CH_3CO	−2.39	α-C on atop	1.975	
CH_2CO	−1.22	both C on atop	2.064, 2.107	
CHCO	−3.32	α-C on atop and β-C on bridge over hcp site	α: 2.076 β: 2.056, 2.082	
CH_3CH_2OH	−0.35	atop		2.391
CH_3CH_2O	−2.24	bridge		2.157, 2.224
CH_2CH_2O	−3.61	β-C on atop and O on bridge over hcp site	2.149, 2.176	2.114
CH_2CH_2OH	−1.82	atop	2.114	
CH_2CHOH	−0.87	π C−C bond on atop	2.176, 2.253	
CH_3CHOH	−1.59	α-C on atop	2.106	
CH_3COH	−2.83	α-C on atop	1.919	
CH_2COH	−3.01	α-C on bridge and β-C on atop over hcp site	α: 2.097, 2.105 β: 2.105	

[a] α and β carbon atom positions are used to specify the configuration details of $C_\beta H_x-C_\alpha H_y-O$ intermediates. Adsorption energies are calculated with respect to intermediates in vacuum. H and O chemisorption energies with respect to H_2/O_2 molecules are quoted in parentheses.

dyne (COH) chemisorb via the unsaturated carbon atom on Rh sites such that the saturated hydroxyl (OH) points away from the metal surface. C_2 oxygenates with saturated OH groups chemisorb via either one or both carbon atoms on Rh terraces, depending on their unsaturation. For adsorbed CH_3CHO, both α-carbon and oxygen atoms bind on atop sites. Adsorption via β-carbon and oxygen atoms is determined to be a stable binding geometry for CH_2CH_2O oxametallacycle, and similar configurations are found for other C_2 oxygenates with unsaturated β-carbon and oxygen atoms.

Rh Stepped Surface. Adsorption sites on the Rh(211) step edge are preferred and result in stronger BEs since the corresponding metal atoms have low coordination (= 7) as compared to Rh terraces (= 9). Atomic hydrogen, oxygen, and OH intermediates adsorb on bridge sites on the Rh step edge,

while atomic carbon and CH species block the Rh(100) step by binding to the hollow site. Closed shell molecules such as CH_3OH and CH_3CH_2OH adsorb on atop sites on the Rh step edge. In general, the binding configurations for C_1 and C_2 intermediates on stepped Rh are similar to Rh terraces but are positioned on step edge sites except for ketene (CH_2CO), bound via β-carbon on the step edge-bridge site and oxygen atom on an atop site.

Microcalorimetric[45] and high-resolution core level photoemission measurements[46] show CO adsorption on Rh/SiO_2 to be in the range of 1.50−1.65 eV. DFT studies report atop site preference for CO adsorption on Rh(111)[45] and Rh(211) step edges.[41] Hence, our results are in agreement with existing CO adsorption reports. DFT-based BEs for CH_x on Rh(111) in the literature[33,47] and those in our study are determined to be within

TABLE 2: BEs and Bond Distances (Rh−C and Rh−O) for Intermediates on the Rh(211) Surface[a]

	BE (eV)	configuration	d_{Rh-C} (Å)	d_{Rh-O} (Å)
C	−7.57	hollow	1.976, 1.976, 1.992, 1.992	
H	−2.70 (−0.60)	bridge-SE	Rh−H: 1.780, 1.780	
O	−5.37 (−2.31)	bridge-SE		1.908, 1.908
CO	−2.03	atop-SE	1.850	
CH	−7.16	hollow	2.104, 2,107, 2.111, 2.117	
CH$_2$	−4.28	bridge-SE	2.029, 2.030	
CH$_3$	−2.21	atop-SE	2.080	
OH	−3.62	bridge-SE via O		2.126, 2.129
CH$_3$OH	−0.57	atop-SE via O		2.330
CH$_3$O	−2.84	bridge-SE via O		2.099, 2.136
CH$_2$O	−1.31	C and O on atop-SE	2.118	1.998
CHO	−2.84	C and O on atop-SE	1.939	2.186
CH$_2$OH	−2.30	atop-SE via C	2.082	
CHOH	−3.49	bridge-SE via C	2.043, 2.053	
COH	−4.59	hcp-SE via C	2.007, 2.008, 2.016	
CH$_3$CHO	−1.12	α-C and O on atop-SE	2.106	2.100
CH$_2$CHO	−2.65	β-C on atop-T and O on bridge-SE	2.137	2.200, 2.213
CH$_3$CO	−2.86	α-C and O on atop-SE	1.963	2.182
CH$_2$CO	−1.71	β-C on atop-SE, α-C on bridge-SE, and O on atop-T over hcp-SE	α: 2.062, 2.226 β: 2.197	2.160
CHCO	−3.55	β-C on bridge-SE	2.129, 2.162	
CH$_3$CH$_2$OH	−0.63	atop-SE		2.280
CH$_3$CH$_2$O	−2.73	bridge-SE		2.087, 2.097
CH$_2$CH$_2$O	−4.12	β-C on atop-T and O on bridge-SE over hcp-SE	2.114	2.116, 2.121
CH$_2$CH$_2$OH	−2.14	atop-SE	2.094	
CH$_2$CHOH	−1.56	π C−C bond on atop-SE	2.143, 2.268	
CH$_3$CHOH	−2.24	α-C and O on atop-SE	2.096	2.234
CH$_3$COH	−3.19	α-C on atop-SE		1.902
CH$_2$COH	−3.31	both C on atop-SE	α: 1.924 β: 2.115	

[a] SE, T, and LE refer to step edge, (111) terrace, and lower edge, respectively, as indicated in Figure 1.

DFT error, and the configurations are also consistent. Weak binding for both CH$_3$OH and CH$_3$CH$_2$OH adsorption on atop sites has been reported on Rh(111),[33] Pt(111),[48] and other transition metals.[49,50] CH$_x$O and CH$_x$OH chemisorption geometries on (111) surfaces of other transition metals[32,48,50] agree well with the configurations determined in this study. Our results closely match geometries for CH$_x$O and CH$_3$CH$_x$O on Rh(111) reported by Choi et al.,[33] except for CH$_3$CHO. Aldehyde and ketone binding on the clean Rh(111) surface is experimentally reported to involve η^2 configuration with both carbon and oxygen atoms of the carbonyl group interacting with the metal surface.[51,52] We have found η^2 configuration for CH$_3$CHO to be more strongly bound on both Rh(111) and Rh(211) surfaces. The ground state configuration determined in this study for CH$_2$CH$_2$O intermediate is also in agreement with the oxametallcyclic structure reported in the literature.[52,53]

Pathways to C$_1$ and C$_2$ Oxygenates on Rh(111) and Rh(211). To determine the reaction routes from activated CO to CH$_3$OH and CH$_3$CH$_2$OH on Rh, we computed the relevant C−H, C−C, C−O, and O−H bond formation barriers (Tables 3 and 4). We first examined the TSs for elementary reactions leading to CO activation in Figure 2, followed by CH$_3$OH formation in Figures 3 and 4 and reactions forming CH$_3$CH$_2$OH in Figures 7−9.

Direct and Hydrogen-Assisted CO Dissociation Pathways. We examined four main routes leading to C−O scission on Rh surfaces: direct CO dissociation, CH$_x$O dissociation (x = 1, 2, 3), COH dissociation, and CHOH mechanism. The CHOH mechanism includes parallel paths for CO hydrogenation via CHO and COH to CHOH, followed by C−O scission. The TS structures for these elementary reactions on flat and stepped Rh surfaces are shown in Figure 2. Rh−C and Rh−O bond distances in the TS structure are reported in Table 3 along with

the associated ZPE-corrected activation barrier for the elementary reaction.

Most of the C−O bond-breaking reactions are exothermic on flat and stepped Rh surfaces and correspond to late TS configurations. At the TS for direct CO dissociation (Figure 2a) on Rh(111), atomic carbon and oxygen sit on hcp and bridge sites. For C−O scission within partially hydrogenated CO, TS structures show a shift for the C terminal from 3-fold hollow (COH) to bridge (CHO and CHOH) and finally atop sites (CH$_2$O and CH$_3$O) on the Rh(111) surface (Figure 2b−f). The binding configuration within the TS for CH$_3$O dissociation is also in agreement with a previously reported study on Rh(111).[33] C−O bond-breaking reactions occur more favorably on step edge sites of the Rh(211) surface as shown in Figure 2g−l. Both CO and CHOH dissociation reactions (Figure 2g,l) proceed across the (100) step such that C/CH sits on the fcc site on the lower terrace, while O/OH adsorbs on the bridge position on the step edge. COH dissociation on Rh(211) involves C atom bound to a 3-fold hollow site near the step edge and OH adsorbed on the step-edge atop site (Figure 2k). At the TS for CH$_x$O dissociation, CH$_x$ moves from hcp (x = 1; Figure 2h) to atop sites (x = 2, 3; Figure 2i,j) on the stepped Rh surface.

CO dissociation on the Rh(111) surface corresponds to a barrier of 2.82 eV with respect to the chemisorbed state; therefore, alternative activation pathways were investigated. Previous theoretical studies have shown that hydrogen accelerates the CO dissociation process by forming partially hydrogenated COH and CH$_x$O species followed by C−O scission on Co(0001),[54−56] Ni(111),[57] Fe,[58] Fe$_x$C,[59,60] and MoS$_2$ surfaces.[61] Formyl (CHO) dissociation to give CH on Rh(111) requires a high activation barrier of 1.15 eV. Instead, hydrogenation of CHO to formaldehyde (CH$_2$O) and CH$_3$O is found to be kinetically more favorable (Table 3). Both of these CH$_x$O species
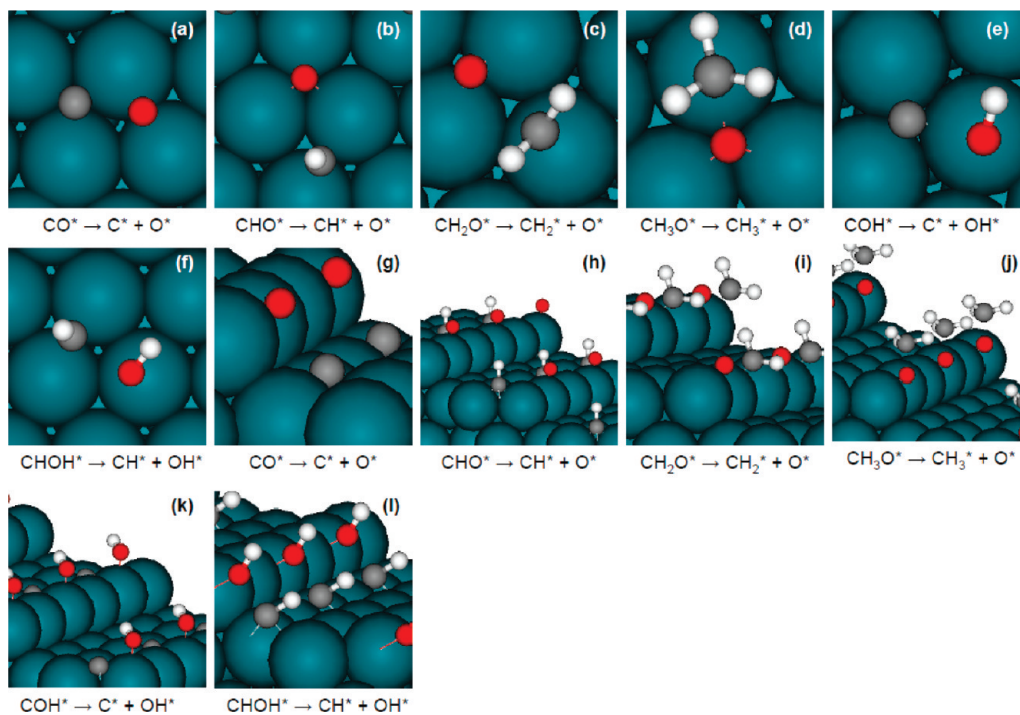
Figure 2. TS structures for CO dissociation reactions on Rh(111) (a–f) and Rh(211) (g–l) surfaces.

TABLE 3: Kinetic Barriers (E_a), Reaction Enthalpy (H), and TS Parameters for C–H, C–O, and O–H Bond Formation Reactions Leading to CO Dissociation and CH$_3$OH Formation on Rh(111) and Rh(211) Surfaces

	E_a (eV)	H (eV)	d_{Rh-C} (Å)	d_{Rh-O} (Å)	d_{Rh-H} (Å)	$d_{reacting\ atoms}$ (Å)
			Rh(111)			
CO(g) → C* + O*	1.07	−0.37	1.90, 1.97, 2.00	2.04, 2.08		1.92
CHO* → CH* + O*	1.15	0.07	1.85, 1.97	1.99, 2.07, 2.09		2.45
CH$_2$O* → CH$_2$* + O*	1.08	0.25	1.91	2.05, 2.05		2.17
CH$_3$O* → CH$_3$* + O*	1.06	−0.19	2.45	2.10, 2.13, 2.13		1.90
COH* → C* + OH*	1.48	0.57	1.89, 1.90, 2.0	2.10		2.19
CHOH* → CH* + OH*	0.55	−0.36	1.94, 1.95	2.09		2.14
CO* + H* → CHO*	1.01	0.81	2.01, 2.31		2.10	1.16
CO* + H* → COH*	1.34	0.64	2.02, 2.02, 2.05		1.82	1.33
CHO* + H* → CHOH*	0.57	0.27	1.95		1.72	1.41
COH* + H* → CHOH*	0.46	0.43	2.05, 2.05, 2.12		1.66	1.37
CHO* + H* → CH$_2$O*	0.28	0.13	2.13, 2.23	2.13	1.64	1.50
CH$_2$O* + H* → CH$_3$O*	0.59	0.15		2.23	1.63	1.98
CH$_3$O* + H* → CH$_3$OH*	0.48	−0.30		2.29, 2.33	1.68	1.48
CHOH* + H* → CH$_2$OH*	0.29	−0.02	2.09, 2.22		1.62	1.53
CH$_2$OH* + H* → CH$_3$OH*	0.47	−0.26	2.31		1.67	1.55
CH$_2$O* + H* → CH$_2$OH*	0.60	0.11	2.14	2.19	1.71	1.53
CH$_3$* + OH* → CH$_3$OH*	1.38	0.06	2.09	2.12		1.96
			Rh(211)			
CO(g) → C* + O*	−0.16	−1.16	1.90, 1.96, 1.96	1.97, 1.97		2.11
CHO* → CH* + O*	1.91	−0.08	1.96, 1.98, 2.19	1.86		2.00
CH$_2$O* → CH$_2$* + O*	1.41	−0.05	1.97	2.01, 2.06		1.89
CH$_3$O* → CH$_3$* + O*	1.16	−0.35	2.34	1.96, 2.01		1.91
COH* → C* + OH*	1.19	−0.25	1.89, 1.92, 1.96	2.11		2.06
CHOH* → CH* + OH*	0.83	−0.84	2.02, 2.02, 2.19	2.22, 2.23		1.74
CO* + H* → CHO*	1.13	0.76	1.90		2.17	1.16
CO* + H* → COH*	0.98	0.87	1.96, 1.96		1.92	1.20
CHO* + H* → CHOH*	0.94	0.51	1.94		1.68	1.45
COH* + H* → CHOH*	0.51	0.39	1.93, 1.97		1.65	1.46
CHO* + H* → CH$_2$O*	0.38	0.21	1.99	2.18	1.65	1.54
CH$_2$O* + H* → CH$_3$O*	0.54	0.07	2.28	2.02	1.60	1.67
CH$_3$O* + H* → CH$_3$OH*	0.96	0.18		2.19	1.64	1.44
CHOH* + H* → CH$_2$OH*	0.0	−0.11	2.09, 2.13		1.64	1.53
CH$_2$OH* + H* → CH$_3$OH*	0.78	0.07	2.28		1.69	1.52
CH$_2$O* + H* → CH$_2$OH*	1.04	0.18	2.10	2.18	1.62	1.49
CH$_3$* + OH* → CH$_3$OH*	2.11	0.79	2.55	2.24, 2.25		1.90

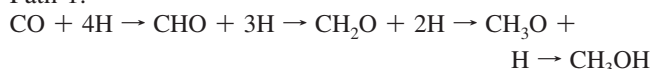($x = 2, 3$) correspond to similar C–O dissociation barriers (1.08 and 1.06 eV). COH dissociation is endothermic on a flat Rh surface with an even higher barrier of 1.48 eV. The lowest C–O scission barrier (0.55 eV) is obtained for CHOH, which results

in exothermic CH and OH formation. CHOH can form via CHO or COH on Rh surfaces. The kinetic barrier for CO + H → CHO is lower than CO + H → COH on the Rh(111) surface, even though COH formation is favored thermodynamically. This reaction is followed by CHO hydrogenation to CHOH such that the C−O bond elongates to 1.37 Å in comparison to 1.16 Å in chemisorbed CO. Hence, the CHOH mechanism for CO activation on flat Rh terraces involves CO + 2H → CHO + H → CHOH → CH + OH. H-assisted CO dissociation is, therefore, determined to be the preferential route for CO activation on Rh(111).

TS structures on Rh(211) involve species bound to step edge sites such that undercoordinated metal atoms stabilize the geometries. Products from bond-breaking reactions on Rh steps are stabilized to a greater degree as opposed to reactants leading to higher exothermicity, as evidenced in Table 3. TS configurations are also lowered in energy on Rh defects, leading to lower kinetic barriers for activation reactions. Direct C−O scission on these Rh defect sites is barrierless, and the atomic products bind on 3-fold sites on the step edge and lower edge of Rh(211) (Figure 2g). Alternative CHOH-, CH$_x$O-, and COH-based C−O scission mechanisms on Rh defect sites correspond to comparatively high barriers and can be ruled out. Hence, direct CO dissociation is favored on step sites both kinetically and thermodynamically. Although atomic carbon binds strongly on Rh(211) step sites (BE on the step edge-hcp site and on the hollow site differs by 0.15 eV), hydrogenation barriers to CH$_x$ are less than 0.6 eV (Table 3 and Figure 1 of the Supporting Information). This result suggests that Rh(211) step sites are not blocked by CO dissociation products and can continue to participate in propagation reactions.

Routes to CH$_3$OH on Rh. Hydrogen addition is mainly investigated as part of syngas to CH$_3$OH routes in this study. Figures 3 and 4 show the routes examined for syngas conversion to CH$_3$OH on Rh(111) and Rh(211) surfaces. Pathways include hydrogenation of undissociated CO via two routes:

Path 1:
$$CO + 4H → CHO + 3H → CH_2O + 2H → CH_3O + H → CH_3OH$$

Path 2:
$$CO + 4H → COH + 3H → CHOH + 2H → CH_2OH + H → CH_3OH$$
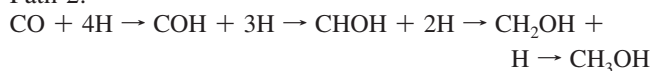
Reactions interlinking these pathways include CHO + H → CHOH and CH$_2$O + H → CH$_2$OH. We also included C−O coupling reactions in this examination: CH$_x$ + O → CH$_x$O (x = 1, 2, 3) and CH$_3$ + OH → CH$_3$OH for comparison against pathways originating from undissociated CO.

TS geometries for C−H and O−H bond formation on Rh(111) and Rh(211) involve atomic hydrogen on an atop metal site as shown in Figures 3 and 4. In most of the C−H bond formation reactions, TS structures involve atomic hydrogen sharing a metal atom with the carbon terminal (Figures 3 and 4a,c,e,f,h,i). At the TS for CO + H → CHO (Figure 3a) and CO + H → COH (Figure 3b) on Rh terraces, CO adsorbs on bridge and hcp sites, respectively. TSs for further hydrogenation of CHO and COH to CHOH (Figure 3c,d) involve CHO at the atop position, while COH sits on hcp sites on the Rh(111) surface. The TS for O−H bond formation in CH$_2$O + H → CH$_2$OH requires CH$_2$O adsorption via both C and O atoms with atomic hydrogen on an adjacent atop site (Figure 3j). At the TS for a CH$_3$ + OH → CH$_3$OH coupling reaction, both adsorbates bond to adjacent atop sites on the Rh(111) surface (Figure 3k).

These C−H and O−H hydrogenation reactions proceed on step edge sites of the Rh(211) surface. CO sits on atop (Figure 4a) and bridge sites (Figure 4b) within the TSs for CHO and COH formation on stepped Rh, respectively. However, at the TS for CO + H → COH, atomic hydrogen adsorbs on the atop site on the lower terrace of the Rh(211) surface. TSs for CHO + H → CHOH (Figure 4c) and COH + H → CHOH (Figure 4d) involve sites on the step edge such that CHO adsorbs on

CO* + H* → CHO*   CO* + H* → COH*   CHO* + H* → CHOH*   COH* + H* → CHOH*

CHO* + H* → CH$_2$O*   CH$_2$O* + H* → CH$_3$O*   CH$_3$O* + H* → CH$_3$OH*   CHOH* + H* → CH$_2$OH*

CH$_2$OH* + H* → CH$_3$OH*   CH$_2$O* + H* → CH$_2$OH*   CH$_3$* + OH* → CH$_3$OH*
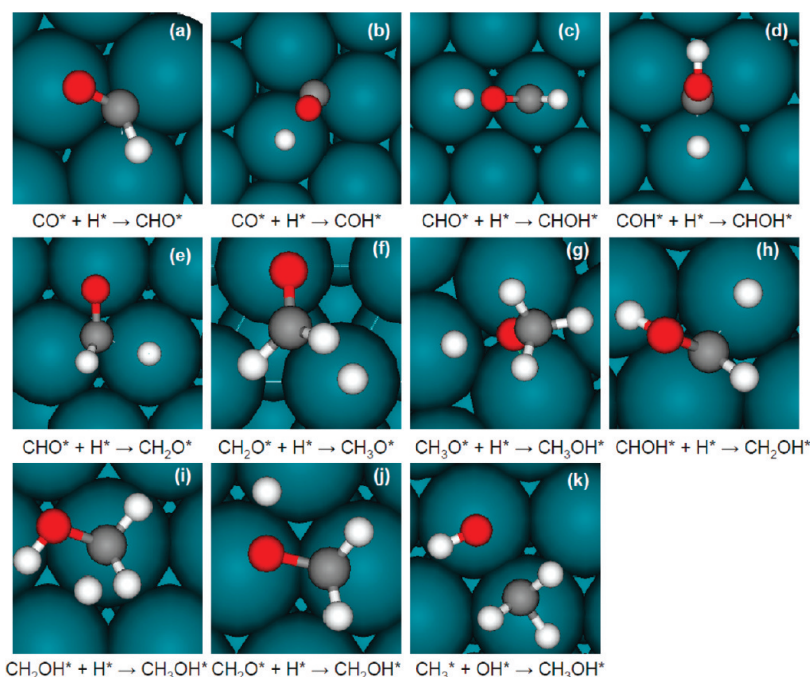
Figure 3. TS structures for CH$_3$OH formation routes on the Rh(111) surface.

Reduced Rh Terraces and Stepped Surfaces

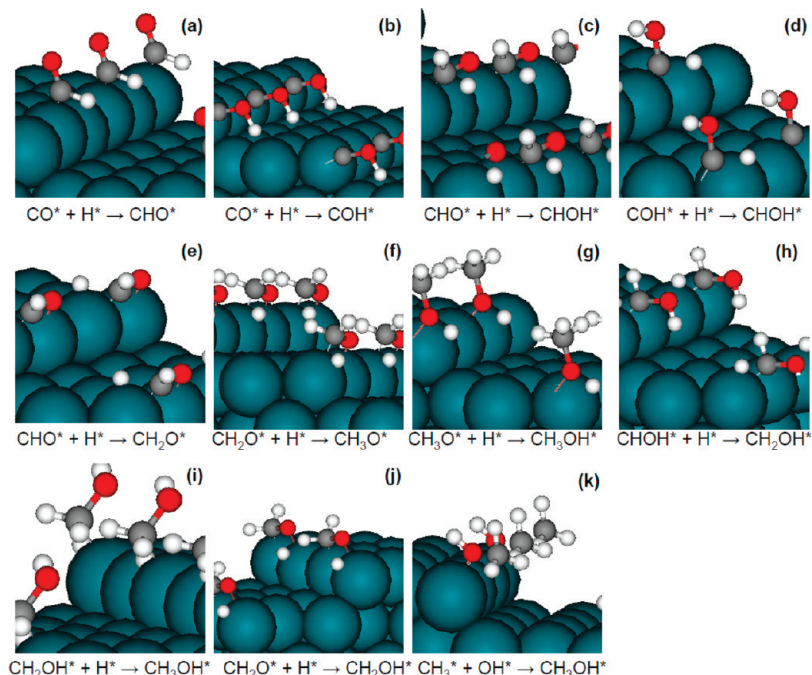*J. Phys. Chem. C, Vol. 114, No. 22, 2010* **10177**

Figure 4. TS structures for CH_3OH formation routes on the Rh(211) surface.
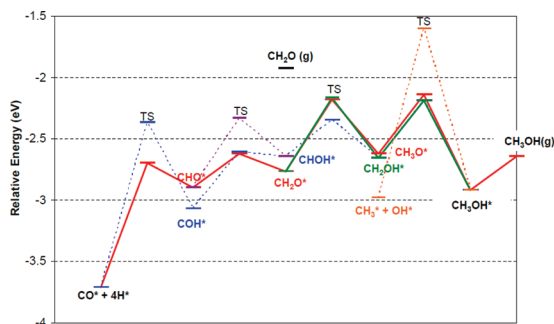

Figure 5. Reaction pathways from syngas to CH_3OH on Rh terraces. Dashed lines represent different routes considered, and solid lines represent the lowest energy pathway. The energy on the *y*-axis is referenced to gas phase CO and $2H_2$.
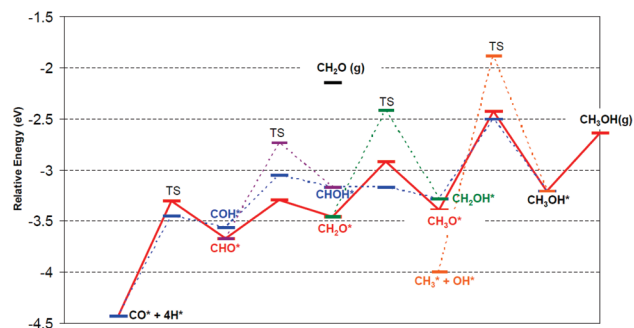

Figure 6. Reaction pathways from syngas to CH_3OH on the Rh(211) surface. Plot details are the same as in Figure 5.

an atop site, while COH adsorbs on a bridge site. Further hydrogenation involves TS structures with equivalent sites on the step edge for CH_3OH formation (Figure 4) with two exceptions: $CH_2O + H \rightarrow CH_3O$ and $CH_3 + OH \rightarrow CH_3OH$.

For hydrogenating the carbon end of CH_2O on Rh(211) (Figure 4f), the TS structure involves C and O terminal bound to step edge-atop sites and atomic hydrogen on shared step edge-atop sites. Figure 4k shows the TS for the C−O coupling reaction wherein CH_3 sits on step edge-atop and OH species bind to step edge-bridge sites.

Although COH binds 0.2 eV more strongly than CHO, the $CO + H \rightarrow CHO$ reaction is kinetically favored on the Rh(111) surface (Figure 5). Adding a hydrogen atom to the carbon end of CHO results in energetically stable CH_2O species on flat Rh terraces and requires a lower energy barrier of 0.28 eV instead of 0.57 eV for $CHO + H \rightarrow CHOH$. Similar activation barriers are required for $CH_2O + H \rightarrow CH_3O$ and $CH_2O + H \rightarrow CH_2OH$ (= 0.59 and 0.60 eV), and both of the reactions are equally likely with similar reaction enthalpies. CH_2O formed can also undergo desorption on Rh(111) since BE equals 0.84 eV. CH_3OH formation can proceed via parallel hydrogenation of CH_3O and CH_2OH intermediates with identical barriers of 0.47 eV. Alternative C−O coupling reactions ($CH_x + O$, $CH + OH$,

and $CH_3 + OH$) on Rh correspond to high energy TSs and are kinetically unfavorable. These CH_x intermediates instead prefer to form methane (Table 3 of the Supporting Information). Hence, CH_3OH and CH_2O formation on Rh(111) entails $CO + 4H \rightarrow CHO + 3H \rightarrow CH_2O + 2H \rightarrow CH_3O/CH_2OH + H \rightarrow CH_3OH$.

Experiments show that CH_2O decomposes on the Rh single crystal surface at temperatures less than 100 K to form adsorbed CO and hydrogen atoms.[51] This experimental result is in agreement with the strong adsorption and low dissociation barriers determined for CH_2O and CHO to form CO on Rh(111). Dissociative CH_3OH adsorption is reported on Rh flat surfaces to form CH_3O species detected with TPD and HREELS.[51] This experimental observation can also be explained with our DFT studies wherein CH_3O formation is favored thermodynamically.

In contrast to Rh(111), CHO and COH have similar BEs and kinetic barriers for formation on Rh(211) (Figure 6). Hydrogen addition to CHO to form CH_2O is less endothermic and has a low barrier (0.38 eV); hence, CH_2O on Rh(211) proceeds through a $CO + 2H \rightarrow CHO + H \rightarrow CH_2O$ mechanism. CH_3O formation from CH_2O is kinetically preferred, followed by O−H bond formation to CH_3OH with a barrier of 0.96 eV on Rh(211). BEs for CH_3OH on Rh(111) and Rh(211) surface equal 0.28 and 0.57 eV, which suggests that CH_3OH desorption is preferred over C−O, C−H, and O−H activation within CH_3OH. TS structures for alternative C−O coupling reactions examined on

TABLE 4: Kinetic Barriers (E_a), Reaction Enthalpy (H), and TS Parameters for C−H, C−C, and O−H Bond Formation Reactions Leading to C$_2$ Oxygenates on the Rh(111) Surface (Subsection A) and Rh(211) Surface (Subsection B)

	E_a (eV)	H (eV)	d_{Rh-C} (Å)	d_{Rh-O} (Å)	d_{Rh-H} (Å)	$d_{reacting\ atoms}$ (Å)
			subsection A			
CH* + CO* → CHCO*	1.01	0.71	2.037, 2.040, 2.098 (CH)	2.045 (CO)		1.75
CH$_2$* + CO* → CH$_2$CO*	0.94	0.35	2.090, 2.250 (CH$_2$)	2.040, 2.051 (CO)		1.84
CH$_3$* + CO* → CH$_3$CO*	1.31	0.12	2.321 (CH$_3$)	2.080, 2.081 (CO)		1.86
CH$_2$CO* + H* → CH$_3$CO*	0.45	−0.52	2.213 (C*), 2.021 (CH$_2$)		1.620	1.55
CH$_3$CO* + H* → CH$_3$CHO*	0.57	0.43	2.069	2.223	1.697	1.37
CH$_2$CO* + H* → CH$_2$CHO*	0.17	0.01	2.132 (C*), 2.197 (CH$_2$)	2.179	1.616	1.61
CH$_2$CHO* + H* → CH$_3$CHO*	0.37	−0.09	2.306 (C*), 2.310 (CH$_2$)	2.143	1.735	1.49
CH$_3$CO* + H* → CH3COH*	0.70	0.44	1.991		1.705	1.44
CH$_3$COH* + H* → CH$_3$CHOH*	0.34	0.19	1.996		1.716	1.56
CH$_3$CHO* + H* → CH$_3$CHOH*	0.67	0.20	2.171	2.196	1.711	1.50
CH$_3$CHOH* + H* → CH$_3$CH$_2$OH*	0.28	−0.43	2.36		1.652	1.66
CH$_2$CHO* + H* → CH$_2$CH$_2$O*	0.40	0.31	2.123	2.132	1.660	1.59
CH$_2$CHO* + H* → CH$_2$CHOH*	0.65	0.17	2.2205		1.708	1.44
CH$_2$CH$_2$O* + H* → CH$_3$CH$_2$O*	0.32	−0.41	2.233	2.153, 2.227	1.628	1.63
CH$_3$CHO* + H* → CH$_3$CH$_2$O*	0.42	0.0		2.194	1.650	1.74
CH$_3$CH$_2$O* + H* → CH$_3$CH$_2$OH*	0.50	−0.21		2.101	1.689	1.60
CH$_2$CH$_2$O* + H* → CH$_2$CH$_2$OH*	0.71	−0.05		2.28, 2.24	1.747	1.34
CH$_2$CH$_2$OH* + H* → CH$_3$CH$_2$OH*	0.38	−0.58	2.256		1.653	1.60
			subsection B			
CH* + CO* → CHCO*	1.67	1.00	1.916, 1.916 (CH)	2.115, 2.115 (CO)		2.06
CH$_2$* + CO* → CH$_2$CO*	0.73	0.56	2.082, 2.186 (CH$_2$)	1.874 (CO)		1.81
CH$_3$* + CO* → CH$_3$CO*	1.34	0.40	2.340 (CH$_3$) 2.042, 2.167	1.848 (CO)		1.90
CH$_2$CO* + H* → CH$_3$CO*	0.28	−0.39	(C*): 2.227 (CH$_2$)	2.194	1.675	1.54
CH$_3$CO* + H* → CH$_3$CHO*	0.48	0.42	2.023	2.159	1.657	1.48
CH$_2$CO* + H* → CH$_2$CHO*	0.39	0.06	2.090 (C*), 2.179 (CH$_2$)	2.151	1.643	1.58
CH$_2$CHO* + H* → CH$_3$CHO*	0.61	−0.04	2.262	2.123	1.599	1.64
CH$_3$CO* + H* → CH3COH*	1.06	0.66	1.971		1.687	1.45
CH$_3$COH* + H* → CH$_3$CHOH*	0.55	0.01	1.976		1.860	1.46
CH$_3$CHO* + H* → CH$_3$CHOH*	1.09	0.25	2.153	2.196	1.742	1.39
CH$_3$CHOH* + H* → CH$_3$CH$_2$OH*	0.68	0.05	2.257	1.620	1.620	1.51
CH$_2$CHO* + H* → CH$_2$CH$_2$O*	0.73	0.45	2.119	2.086	1.643	1.66
CH$_2$CHO* + H* → CH$_2$CHOH*	1.03	0.13	2.161 (CH$_2$); 2.253 (CH)		1.737	1.39
CH$_2$CH$_2$O* + H* → CH$_3$CH$_2$O*	0.29	−0.28	2.228	2.129, 2.137	1.631	1.63
CH$_3$CHO* + H* → CH$_3$CH$_2$O*	0.60	0.20		2.046	1.607	1.70
CH$_3$CH$_2$O* + H* → CH$_3$CH$_2$OH*	0.79	0.10		2.075	1.726	1.53
CH$_2$CH$_2$O* + H* → CH$_2$CH$_2$OH*	0.95	0.25	2.130 (β-CH$_2$)	2.219, 2.248	1.648	1.41
CH$_2$CH$_2$OH* + H* → CH$_3$CH$_2$OH*	0.44	−0.43	2.240		1.674	1.56

Rh step sites correspond to higher energy as compared to TSs for the preferred CH$_x$O-based route. On the basis of our findings, we can conclude that CH$_2$O and CH$_3$OH formation involves hydrogen addition to the carbon end of undissociated CO on stepped Rh such that CO + 4H → CHO + 3H → CH$_2$O + 2H → CH$_3$O + H → CH$_3$OH. On flat surfaces, CO can hydrogenate to CH$_3$OH via parallel mechanisms involving CH$_3$O and hydroxyl methyl (CH$_2$OH) species. The preference for CH$_x$O-based intermediates for CH$_2$O and CH$_3$OH formation has been reported previously on cobalt step sites,[32] Pd(111),[50] and Ni(111),[49] while alternative routes involving COH intermediates and C−O bond-breaking steps have been invoked for CH$_3$OH decomposition routes on Pt(111)[48,62] and Pd(111)[63] surfaces. This nondissociative, CO hydrogenation mechanism to CH$_3$OH determined for Rh surfaces agrees with isotopic tracer studies reported in the literature.[29] Inspite of the similar reaction mechanism on Rh(111) and Rh(211), CH$_3$OH formation is structure sensitive with lower energy states on Rh defects (Figures 5 and 6). However, these defects can become less active than Rh terraces in the event of CO poisoning the step sites. The overall rate of the reaction is determined by CH$_3$O + H → CH$_3$OH on Rh(211) and CH$_3$O/CH$_2$OH + H→ CH$_3$OH on Rh(111) since the respective TSs are the highest energy TSs in the pathways.

Routes to CH$_3$CH$_2$OH and CH$_3$CHO on Rh. Higher oxygenate formation on Rh surfaces typically involves CO insertion

in adsorbed monomer species followed by hydrogenation reactions. Atomic carbon resulting from direct CO dissociation on Rh(211) prefers to hydrogenate to CH$_x$ intermediates (Table 3 of the Supporting Information), which act as monomers for chain growth and oxygenate formation. On the Rh terraces, H-assisted CO dissociation involving CHO, CHOH, and COH species has to be invoked for forming CH$_x$ monomer units. Hence, we examined CO insertion into both CH$_x$ and partially hydrogenated CO species (CHO, COH, and CHOH) for C$_2$ oxygenate formation on Rh(111).

Reaction enthalpies for C−C coupling in CO + CHO, CO + COH, and CO + CHOH on the flat Rh surface are determined to be endothermic by 1.06, 0.70, and 0.82 eV, respectively. These reaction energies for CO + CHO, CO + COH, and CO + CHOH remain endothermic on Rh(211) sites by 1.49, 0.95, and 0.74 eV (Figure 2 of the Supporting Information). In comparison, CO insertion into CH$_2$ and CH$_3$ are less endothermic (Table 4a,b) and, therefore, are thermodynamically more favorable for oxygenate formation on flat and stepped Rh surfaces. Activation barriers and TS geometries for CO insertion into CH, CH$_2$, and CH$_3$ intermediates on Rh surfaces are reported in Figure 7 and Table 4, respectively.

In the TSs for CH$_x$ + CO on flat Rh surfaces, CO moves from an atop site (CH + CO) to bridge (CH$_2$ + CO) and finally hcp sites (CH$_3$ + CO). CH$_x$ species also change binding positions from hcp (x = 1, CH + CO) to bridge (x = 2, CH$_2$ +

Reduced Rh Terraces and Stepped Surfaces

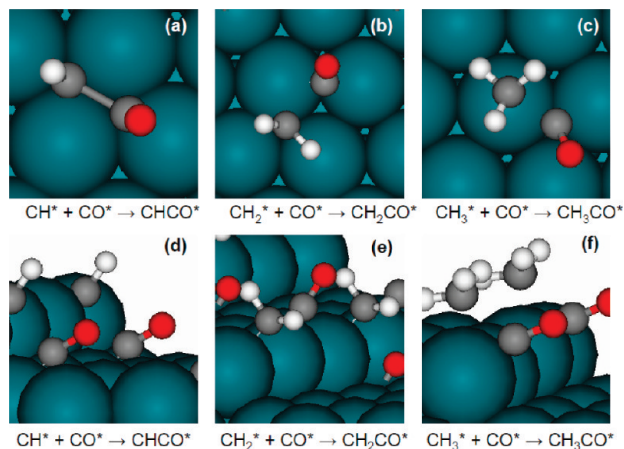*J. Phys. Chem. C, Vol. 114, No. 22, 2010* **10179**

Figure 7. TS structures for CH + CO→ CHCO (a and d), CH₂ + CO→ CH₂CO (b and e), and CH₃ + CO → CH₃CO (c and f) on Rh(111) and Rh(211) surfaces.

TABLE 5: BEs for C₂HᵧO_z Intermediates on Rh(111) and Rh(211) with Respect to Atomic Carbon, Hydrogen, and Oxygen in Vacuum
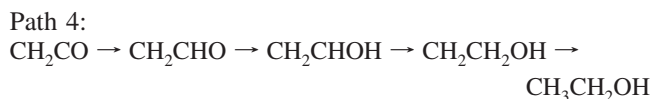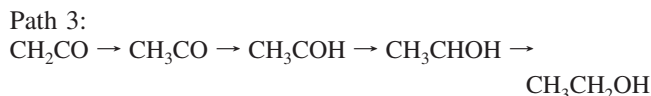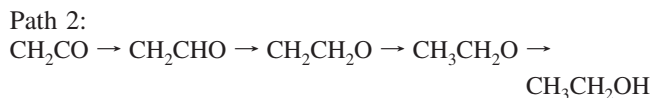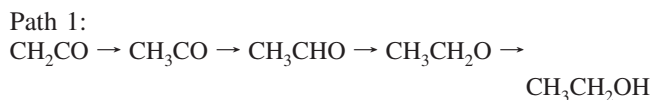
stoichiometric ratios	species	BE/Rh(111) (eV)	BE/Rh(211) (eV)
C₂H₃O	CH₃CO	−28.79	−29.26
	CH₂CHO	−28.27	−28.81
	CH₂COH	−28.10	−28.40
C₂H₄O	CH₃CHO	−30.96	−31.55
	CH₃COH	−30.94	−31.30
	CH₂CHOH	−30.69	−31.38
	CH₂CH₂O	−30.55	−31.06
C₂H₅O	CH₃CH₂O	−33.56	−34.05
	CH₃CHOH	−33.34	−33.99
	CH₂CH₂OH	−33.19	−33.51

CO) and finally atop sites for CH₃ species (*x* = 3, CH₃ + CO) (Figure 7a−c). At the TS for CH + CO on the Rh(211) surface, CH sits on the step edge-bridge and CO sits on the fcc site on the lower edge (Figure 7d). For CO insertion into CH₂ and CH₃, TSs on stepped Rh include CO chemisorbed on step edge-atop sites with either CH₂ on the step edge-bridge (Figure 7e) or CH₃ on the step edge-atop site (Figure 7f).

CO insertion into CH and CH₂ corresponds to a similar barrier (c.a. 1 eV), but CH₂CO formation is less endothermic and, hence, preferred for oxygenate formation on flat Rh. Significant barrier reduction is determined for CO insertion into CH₂ on defect sites unlike alternative insertion reactions (CH + CO and CH₃ + CO) with high kinetic constraints. Experimental reports have also previously claimed CH₂ as a key reaction intermediate[64] and reported an increase in C₂ oxygenate product with the addition of methylene (CH₂Cl₂) but not methyl chloride.[31] Thus, CO insertion is most feasible into CH₂ on both Rh(111) and (211) surfaces.

CH₃CH₂OH and CH₃CHO are formed by further hydrogenating CH₂CO intermediates. Species with a stoichiometric ratio beyond C₂H₂O (CH₂ + CO) with hydrogen atom increments to C₂H₅O are considered in Table 5 so as to narrow down potential hydrogenation reactions in the investigation. Intermediates within 0.5 eV of the lowest energy species for C₂HₓO (*x* = 3, 4, 5) stoichiometric ratio are thereby selected. On the basis of this adsorption energy analysis, CH₂COH is excluded from the reaction network for C₂ oxygenates. Experimental studies show that CH₃CH₂OH undergoes dissociative adsorption on Rh single crystals to form ethoxy species.[51] Our calculations confirm this experimentally observed result on Rh(111) and establish ethoxy

as the most stable intermediate formed by hydrogen abstraction from CH₃CH₂OH. Four main routes considered for CH₂CO hydrogenation to CH₃CH₂OH on Rh(111) and Rh(211) include

Path 1:
$$CH_2CO \rightarrow CH_3CO \rightarrow CH_3CHO \rightarrow CH_3CH_2O \rightarrow$$
$$CH_3CH_2OH$$

Path 2:
$$CH_2CO \rightarrow CH_2CHO \rightarrow CH_2CH_2O \rightarrow CH_3CH_2O \rightarrow$$
$$CH_3CH_2OH$$

Path 3:
$$CH_2CO \rightarrow CH_3CO \rightarrow CH_3COH \rightarrow CH_3CHOH \rightarrow$$
$$CH_3CH_2OH$$

Path 4:
$$CH_2CO \rightarrow CH_2CHO \rightarrow CH_2CHOH \rightarrow CH_2CH_2OH \rightarrow$$
$$CH_3CH_2OH$$

Reactions interlinking these four paths include CH₂CHO + H → CH₃CHO and CH₂CHOH + H → CH₃CHOH. These paths differ in the preferential hydrogenation of α-C, β-C, and oxygen atoms in CH₂CO and subsequent hydrogenated intermediates. Because C−C and C−O bonds require high activation barriers as compared to C−H bonds, we have not considered CHₓ + CHᵧOH_z or CHₓCHᵧ + OH_z reactions to form CH₃CH₂OH on both flat and stepped Rh surfaces.

Figures 8 and 9 show the TSs for C−H and O−H bond formation reactions to C₂ oxygenates on Rh terraces and defect sites, respectively. The TS for CH₂CO hydrogenation to acyl (CH₃CO) and CH₂CHO requires coadsorbed atomic hydrogen sharing a metal atom with β-C and α-C of CH₃CO and CH₂CHO adsorbates, respectively, on the Rh(111) surface (Figure 8a,c). At the TS for α-C−H bond formation on the flat Rh surface to CH₂CH₂O, α-C and O atoms are bound to atop sites (Figure 8i) and for β-C−H bond formation, both carbon atoms are bound atop on a metal site (Figure 8d). Oxametallacycle CH₂CH₂O hydrogenates to ethoxy (CH₃CH₂O) through TS wherein β-C and O atoms are bound to atop sites and β-C and atomic hydrogen share the metal atom (Figure 8k). TSs for O−H bond formation reactions on Rh(111) involve CH₂CHO bound via β-C on atop site (Figure 8j), CH₃CO sitting on an atop site through α-C (Figure 8e), CH₃CHO adsorbed via both α-C and O on atop sites (Figure 8g), and CH₂CH₂O binding to atop sites through β-C and O end (Figure 8n) along with coadsorbed atomic hydrogen atop on a metal site on Rh terraces. TSs for other C−H hydrogenation reactions on Rh(111) (Figure 8j,h,o) involve CH₃COH, CH₃CHOH, and CH₂CH₂OH bound via unsaturated carbon atoms on atop sites shared with coadsorbed hydrogen atoms.

As is evident from C−H and O−H bond formation structures leading to CH₃OH, TS geometries determined on Rh(211) for C₂ oxygenate formation are similar to Rh terraces with equivalent sites on the Rh step edge with few exceptions. C−H bond addition to CH₂CH₂O to form CH₃CH₂O on Rh(211) proceeds with O on step edge-bridge and β-C atop on terrace site sharing the metal atom with atomic hydrogen (Figure 9k). For CH₂CHO + H → CH₂CHOH on the stepped Rh surface, reactant CH₂CHO sits with α-C on the step edge-atop and β-C on terrace-atop sites such that an adjacent hydrogen atom adsorbs on the step edge-atop to form O−H bond (Figure 9j).
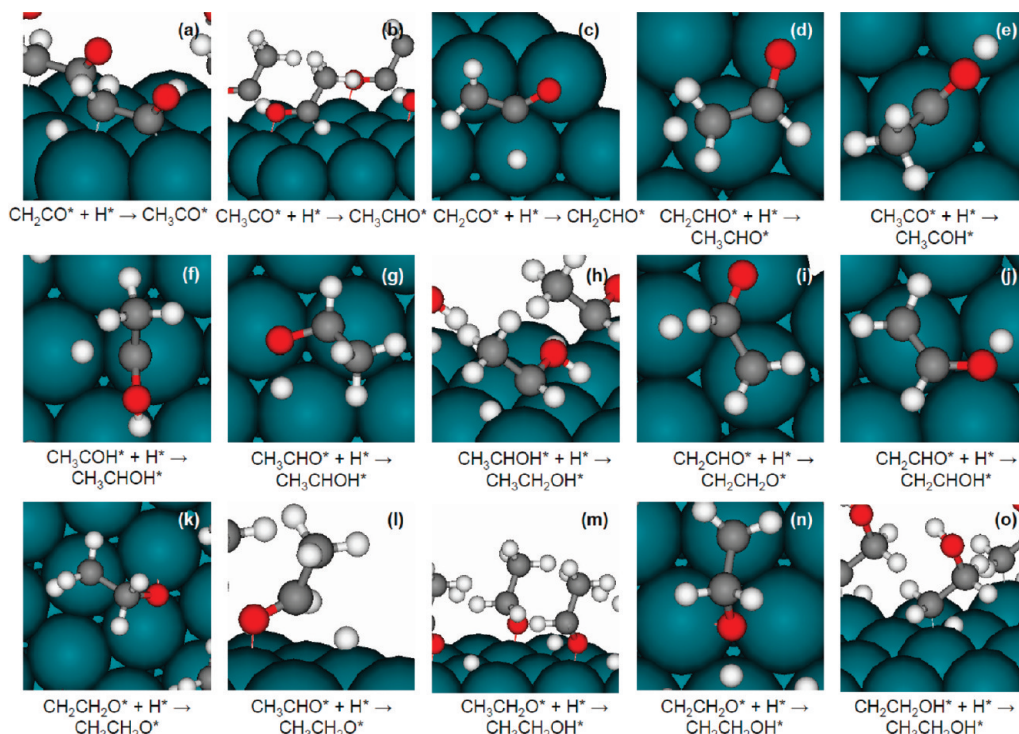
Figure 8. TS structures for C−H and O−H bond formation to C_2−oxygenates on the Rh(111) surface.
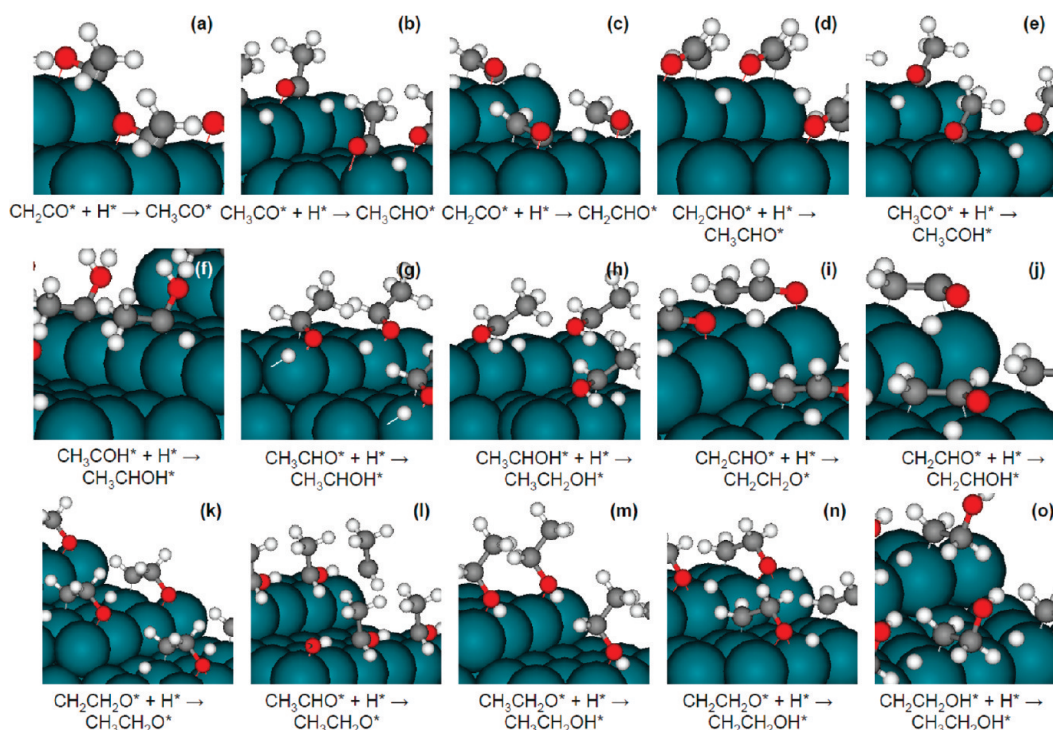

Figure 9. TS structures for C−H and O−H bond formation to C_2−oxygenates on the Rh(211) surface.

Figures 10 and 11 show the reaction energetics for C_2 oxygenate formation on flat and stepped Rh surfaces via feasible reaction routes. Although CH_3CO formation is thermodynamically more favorable, kinetics dictate $CH_2CO + H \rightarrow CH_2CHO$ on Rh(111) (Figure 10). Further hydrogenation of CH_2CHO to CH_2CH_2O and CH_2CHOH intermediates is endothermic, while CH_3CHO formation is slightly exothermic. Nearly identical barriers are determined for CH_2CHO hydrogenation to CH_3CHO and oxametallacycle CH_2CH_2O formation (0.4 eV, Table 4a). CH_3CHO thus formed on Rh(111) is likely to undergo desorption since the barrier equals 0.53 eV. Both CH_3CHO and

CH_2CH_2O can undergo hydrogenation with similar kinetic barriers to form CH_3CH_2O followed by $CH_3CH_2O + H \rightarrow CH_3CH_2OH$ reaction on Rh(111). Other DFT-based studies report sequential hydrogenation of CH_3CO via CH_3CHO intermediate to form CH_3CH_2OH on stepped cobalt sites[32] and routes involving CH_3COH and CH_3CHOH as the interim products for the flat Rh surface.[33]

Although CH_3CHO hydrogenation provides a lower energy route for forming CH_3CH_2OH as compared to CH_2CH_2O hydrogenation, IR and isotopic labeling studies report contradicting results on CH_3CHO as a reactive intermediate for

Reduced Rh Terraces and Stepped Surfaces

J. Phys. Chem. C, Vol. 114, No. 22, 2010 **10181**

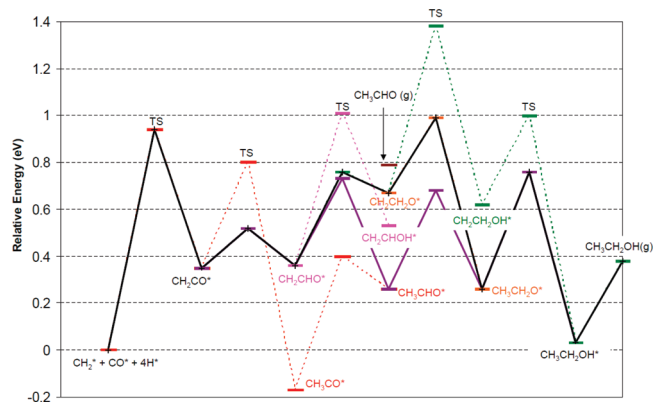**Figure 10.** CO insertion and hydrogenation pathways to CH_3CH_2OH on the Rh(111) surface. Dashed lines represent different routes, and solid lines represent the lowest energy pathway.
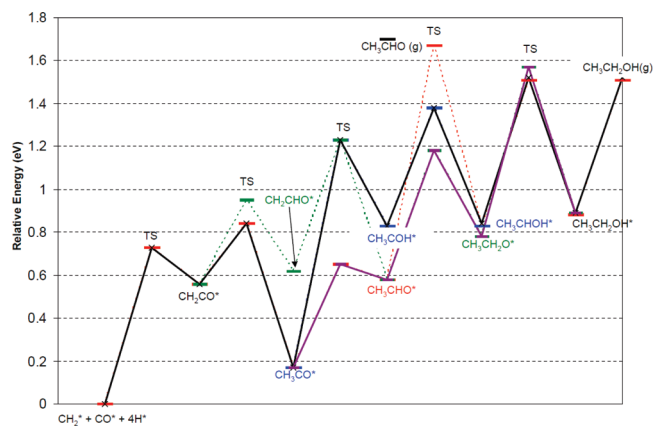

Figure 11. CO insertion and hydrogenation pathways to CH_3CH_2OH on the Rh(211) surface. Dashed lines represent different routes, and solid lines represent the lowest energy pathway.

CH_3CH_2OH formation.[34–36,38,39] CH_3CHO dissociation to CH_3CO is found to be strongly exothermic in our study and requires a low barrier of 0.14 eV. Our calculations confirm acyl as a thermodynamic sink, which is reported to stabilize as acetate ions on supports identified by IR peaks.[38,39] Because acyl/Rh(111) corresponds to an energy well, we have focused on the CH_2CH_2O-based hydrogenation pathway on Rh(111) as a parallel path for CH_3CH_2OH formation. Oxametallacyclic CH_2CH_2O undergoes exothermic β-C hydrogenation to CH_3CH_2O with a barrier of 0.32 eV and further O−H bond formation with a barrier of 0.50 eV to form CH_3CH_2OH. This deduction agrees with CH_3CH_2OH decomposition studies on Rh(111) by Barteau and co-workers,[52,53] in which oxametallacycle intermediate is proposed.

Figure 11 shows the potential CH_3CH_2OH formation routes on stepped Rh surfaces with the same set of C_xH_yO intermediates as considered on Rh(111). In contrast to Rh(111), β-C of CH_2CO is energetically and kinetically favored over α-C for hydrogenation to form CH_3CO on Rh defect sites. Further hydrogenation of CH_3CO leads to CH_3CHO, which requires 1.12 eV to desorb. CH_3CHO dissociation to acyl is exothermic on Rh(211) similar to Rh(111) and proceeds with a negligible barrier. In the absence of CH_3CHO decomposition to acyl, CH_3CHO can hydrogenate to CH_3CH_2O and CH_3CH_2OH. Because of the side reaction for acyl formation, this mechanism is less likely, and other alternative routes are considered. Acyl hydrogenation to CH_3COH corresponds to a barrier of 1.06 eV. Subsequent hydrogen addition to α-C of CH_3COH intermediate on stepped Rh to form CH_3CHOH and CH_3CH_2OH proceeds via endother-

mic reactions with barriers of 0.55 and 0.68 eV, respectively. Thus, structure-sensitive reaction pathways for syngas conversion to CH_3CHO and CH_3CH_2OH are determined on Rh terrace and defect sites, which involve different surface intermediates.

On the basis of this first-principles study, we have determined that the lowest energy pathways for oxygenates are preferred on Rh stepped surfaces due to energetic stabilization of reactants, TSs, and products on low coordinated sites (Figures 5 and 6 and Figure 3 of the Supporting Information). Experimentally, a significant TOF for CO is reported on larger Rh/SiO_2[17,19] nanoparticles[17,19] with high step density.[20,37] High pressure IR studies on highly dispersed Rh/SiO_2 nanoparticles show CO adsorption on step sites (1780 cm⁻¹).[37] As the nanoparticle size increases, this peak shifts to lower frequencies (~1740 cm⁻¹) and overlaps with the acetate peak (1745 cm⁻¹). Hence, one can infer availability of Rh defect sites under operating conditions for syngas conversion. An experimentally observed increase in activity and product selectivity trends can therefore be reconciled with theoretical findings on stepped surfaces in this study. Rh surfaces are typically considered saturated with CO under operating conditions for syngas conversion to oxygenates. Previously reported DFT investigations have shown that apparent dissociation barriers increase with an increase in CO coverage for O_2 dissociation on Pt(111).[65] Conversely, coupling between atomic oxygen atoms becomes less endothermic, and barriers for the recombination reaction decrease with an increase in CO coverage. Hence, we can deduce that dissociation reactions are suppressed, while addition reactions are promoted under high coverage conditions.

We extend these conclusions to dissociation and addition reactions for the CO hydrogenation mechanism on Rh surfaces. For small particles with high dispersion, CO preferentially adsorbs on the step sites, but CO dissociation will be inhibited due to high surface coverage. This explains the low experimental TOF observed for small Rh nanoparticles. As the particle size increases, defects sites are still available as evidenced by IR peaks for CO adsorption on the edge-bridge.[37] Local CO coverage, on the other hand, decreases due to reduced dispersion, and CO dissociation can proceed on Rh defect sites leading to an increase in CO TOF. Because small nanoparticles are mostly covered with CO, few hydrogen molecules are able to bind and dissociate on Rh sites. Atomic hydrogen thus generated can combine with undissociated CO on step sites to selectively form CH_3OH on small nanoparticles. CH_3OH selectivity decreases with an increase in particle size since the CO dissociation rate is improved on bigger Rh particles. CH_3CH_2OH selectivity requires the presence of both CH_2 and CO species; therefore, CH_3CH_2OH yield decreases beyond a critical nanoparticle size. Thus, oxygenate selectivity trends can be inferred based on the competition between C−O, C−H, and C−C bond formation reactions from the above analysis on Rh sites.

Conclusions

Density functional simulations were used to investigate C_1 and C_2 oxygenate formation routes on stepped and flat Rh surfaces. The CH_3OH formation route via CO → CHO → CH_2O → CH_3O/CH_2OH → CH_3OH is kinetically favorable on Rh(111). On Rh steps, CH_2O hydrogenates preferably to CH_3O followed by CH_3OH. The last hydrogen addition step for CH_3OH formation [CH_3O + H on Rh(211) and CH_3O/CH_2OH + H on Rh(111)] involves the highest TS energy and is responsible for limiting the CH_3OH formation rate. Direct CO dissociation is preferred on Rh step sites, while Rh terraces favor a H-assisted CO dissociation mechanism involving the CHOH

10182 *J. Phys. Chem. C, Vol. 114, No. 22, 2010*

Kapur et al.

intermediate. C_2 oxygenate formation proceeds via the CH_2 + CO reaction on Rh surfaces, which is favored both kinetically and thermodynamically. While Rh(111) sites favor CH_2CO hydrogenation via the CH_2CH_2O intermediate, a pathway via CH_3COH species is favored for CH_3CH_2OH formation on Rh(211). CH_3CHO hydrogenation to CH_3CH_2OH on Rh surfaces is kinetically less favorable as compared to exothermic dissociation to strongly bound CH_3CO intermediates. Energy profiles for the mechanistic pathways to oxygenates are lower on stepped surfaces, indicating preference for low coordinated Rh sites.

Supporting Information Available: Additional table and figure for CH_x hydrogenation and energy path comparison for CH_3CH_2OH formation on Rh surfaces. This material is available free of charge via the Internet at http://pubs.acs.org.

References and Notes

(1) Spath, P. L.; Dayton, D. C. NREL/TP-510-34929; December, 2003.
(2) Chuang, S. S. C.; Stevens, R. W.; Khatri, R. *Top. Catal.* **2005**, *32*, 225–232.
(3) Spivey, J. J.; Egbebi, A. *Chem. Soc. Rev.* **2007**, *26*, 1514.
(4) Quyoum, R.; Berdini, V.; Turner, M. L.; Long, H. C.; Maitlis, P. M. *J. Catal.* **1998**, *173*, 355.
(5) Wang, Y.; Song, Z.; Ma, D.; Luo, H.; Liang, D.; Bao, X. *J. Mol. Catal. A* **1999**, *149*, 51.
(6) Ichikawa, M.; Fukushima, T. *J. Chem. Soc. Chem. Commun.* **1985**, 321.
(7) Kawai, M.; Uda, M.; Ichikawa, M. *J. Phys. Chem.* **1985**, *89*, 1654–1656.
(8) Solymosi, F.; Pasztor, M. *J. Phys. Chem.* **1985**, *89*, 4789–4793.
(9) Solymosi, F.; Pasztor, M. *J. Phys. Chem.* **1986**, *90*, 5312–5317.
(10) Basu, P.; Panayotov, D.; Yates, J. T. *J. Phys. Chem.* **1987**, *91*, 3133–3136.
(11) Basu, P.; Panayotov, D.; Yates, J. T. *J. Am. Chem. Soc.* **1988**, *110*, 2074–2081.
(12) Wilson, J.; de Groot, C. *J. Phys. Chem.* **1995**, *99*, 7860–7866.
(13) Beitel, G. A.; de Groot, Cor P. M.; Oosterbeek, H.; Wilson, J. H. *J. Phys. Chem. B* **1997**, *101*, 4035–4043.
(14) Bezemer, G. L.; Bitter, J. H.; Kuipers, H. P. C. E.; Oosterbeek, H.; Holewijn, J. E.; Xu, X.; Kapteijn, F.; van Dillen, A. J.; de Jong, K. P. *J. Am. Chem. Soc.* **2006**, *128*, 3956–3964.
(15) de Jong, A. M.; Niemantsverdriet, J. W. *J. Chem. Phys.* **1994**, *101*, 10126–10133.
(16) Yates, J. J. T.; Worley, S. D.; Duncan, T. M.; Vaughan, R. W. *J. Chem. Phys.* **1979**, *70*, 1225–1230.
(17) Arakawa, H.; Takeuchi, K.; Matsuzaki, T.; Sugi, Y. *Chem. Lett.* **1984**, *13*, 1607.
(18) Hanaoka, T.; Arakawa, H.; Matsuzaki, T.; Sugi, Y.; Kanno, K.; Abe, Y. *Catal. Today* **2000**, *58*, 271.
(19) Zhou, S.; Zhao, H.; Ma, D.; Miao, S.; Cheng, M.; Bao, X. *Z. Phys. Chem.* **2005**, *219*, 949.
(20) Ojeda, M.; Rojas, S.; Boutonnet, M.; Perez-Alonso, F. J.; Garcia-Garcia, F. J.; Fierro, J. L. G. *Appl. Catal., A* **2004**, *274*, 33.
(21) Andersson, S.; Frank, M.; Sandell, A.; Giertz, A.; Brena, B.; Bruhwiler, P. A.; Martensson, N.; Libuda, J.; Baumer, M.; Freund, H. J. *J. Chem. Phys.* **1998**, *108*, 2967–2974.
(22) Frank, M.; Andersson, S.; Libuda, J.; Stempel, S.; Sandell, A.; Brena, B.; Giertz, A.; Brühwiler, P. A.; Bäumer, M.; Martensson, N.; Freund, H. J. *Chem. Phys. Lett.* **1997**, *279*, 92.
(23) Freund, H. J. *Chem. Phys. Lett.* **1999**, *310*, 229.

(24) de Mongeot, F. B.; Toma, A.; Molle, A.; Lizzit, S.; Petaccia, L.; Baraldi, A. *Phys. Rev. Lett.* **2006**, *97*, 056103–056104.
(25) Yates, J. T., Jr.; Williams, E. D.; Weinberg, W. H. *Surf. Sci.* **1980**, *91*, 562.
(26) Rebholz, M.; Prins, R.; Kruse, N. *Surf. Sci.* **1991**, *259*, L797.
(27) Mavrikakis, M.; Bäumer, M.; Freund, H. J.; Nørskov, J. K. *Catal. Lett.* **2002**, *81*, 153–156.
(28) Liu, Z.; Hu, P. *J. Am. Chem. Soc.* **2003**, *125*, 1958–1967.
(29) Takeuchi, A.; Katzer, J. R. *J. Phys. Chem.* **1981**, *85*, 937–939.
(30) Deluzarche, A.; Hindermann, J. P.; Kieffer, R.; Breault, R.; Kiennemann, A. *J. Phys. Chem.* **1984**, *88*, 4993–4995.
(31) Loek, T.; Favre, F.; van der Lee, G.; Ponec, V. *J. Chem. Soc. Chem. Commun.* **1985**, 230.
(32) Cheng, J.; Hu, P.; Ellis, P.; French, S.; Kelly, G.; Lok, C. M. *J. Phys. Chem. C* **2008**, *112*, 9464–9473.
(33) Choi, Y.; Liu, P. *J. Am. Chem. Soc.* **2009**, *131*, 13054–13061.
(34) Orita, H.; Naito, S.; Tamaru, K. *Chem. Lett.* **1983**, *12*, 1161.
(35) Burch, R.; Petch, M. I. *Appl. Catal., A* **1992**, *88*, 61.
(36) Underwood, R. P.; Bell, A. T. *Appl. Catal.* **1986**, *21*, 157.
(37) Arakawa, H.; Fukushima, T.; Ichikawa, M.; Takeuchi, K.; Matsuzaki, T.; Sugi, Y. *Chem. Lett.* **1985**, *14*, 23.
(38) Bowker, M. *Catal. Today* **1992**, *15*, 77.
(39) Orita, H.; Naito, S.; Tamaru, K. *J. Catal.* **1988**, *112*, 176.
(40) Kresse, G.; Furthmüller, J. *Phys. Rev. B* **1996**, *54*, 11169.
(41) Mavrikakis, M.; Rempel, J.; Greeley, J.; Hansen, L. B.; Norskov, J. K. *J. Chem. Phys.* **2002**, *117*, 6737–6744.
(42) Blöchl, P. E. *Phys. Rev. B* **1994**, *50*, 17953.
(43) Monkhorst, H. J.; Pack, J. D. *Phys. Rev. B* **1976**, *13*, 5188.
(44) Henkelman, G.; Jonsson, H. *J. Chem. Phys.* **1999**, *111*, 7010–7022.
(45) He, R.; Kusaka, H.; Mavrikakis, M.; Dumesic, J. A. *J. Catal.* **2003**, *217*, 209.
(46) Smedh, M.; Beutler, A.; Borg, M.; Nyholm, R.; Andersen, J. N. *Surf. Sci.* **2001**, *491*, 115.
(47) Yang, M.; Bao, X.; Li, W. *J. Chem. Phys.* **2007**, *127*, 024705–024710.
(48) Greeley, J.; Mavrikakis, M. *J. Am. Chem. Soc.* **2002**, *124*, 7193–7201.
(49) Remediakis, I. N.; Abild-Pedersen, F.; Norskov, J. K. *J. Phys. Chem. B* **2004**, *108*, 14535–14540.
(50) Neurock, M. *Top. Catal.* **1999**, *9*, 135–152.
(51) Vohs, J. *Adsorbed Layers Surf.* **2003**, 426–439.
(52) Houtman, C. J.; Barteau, M. A. *J. Catal.* **1991**, *130*, 528.
(53) Mavrikakis, M.; Barteau, M. A. *J. Mol. Catal. A* **1998**, *131*, 135.
(54) Zhuo, M.; Tan, K. F.; Borgna, A.; Saeys, M. *J. Phys. Chem. B* **2009**, *113*, 8357–8365.
(55) Inderwildi, O. R.; Jenkins, S. J.; King, D. A. *J. Phys. Chem. C* **2008**, *112*, 1305–1307.
(56) Cheng, J.; Hu, P.; Ellis, P.; French, S.; Kelly, G.; Lok, C. *Top. Catal.* **2010**, *53*, 326.
(57) Andersson, M. P.; Abild-Pedersen, F.; Remediakis, I. N.; Bligaard, T.; Jones, G.; Engbæk, J.; Lytken, O.; Horch, S.; Nielsen, J. H.; Sehested, J.; Rostrup-Nielsen, J. R.; Nørskov, J. K.; Chorkendorff, I. *J. Catal.* **2008**, *255*, 6–19.
(58) Huo, C. F.; Ren, J.; Li, Y. W.; Wang, J.; Jiao, H. *J. Catal.* **2007**, *249*, 174.
(59) Huo, C.; Li, Y.; Wang, J.; Jiao, H. *J. Am. Chem. Soc.* **2009**, *131*, 14713–14721.
(60) Gracia, J. M.; Prinsloo, F. F.; Niemantsverdriet, J. W. *Catal. Lett.* **2009**, *133*, 257–261.
(61) Huang, M.; Cho, K. *J. Phys. Chem. C* **2009**, *113*, 5238–5243.
(62) Greeley, J.; Mavrikakis, M. *J. Am. Chem. Soc.* **2004**, *126*, 3910–3919.
(63) Zhang, C. J.; Hu, P. *J. Chem. Phys.* **2001**, *115*, 7182–7186.
(64) Jackson, S. D.; Brandreth, B. J.; Winstanley, D. *J. Catal.* **1987**, *106*, 464.
(65) Shan, B.; Kapur, N.; Hyun, J.; Wang, L.; Nicholas, J. B.; Cho, K. *J. Phys. Chem. C* **2009**, *113*, 710–715.